International Journal of Adhesion & Adhesives 105 (2021) 102762

Contents lists available at ScienceDirect

International Journal of Adhesion and Adhesives

journal homepage: http://www.elsevier.com/locate/ijadhadh

R-curve behavior of adhesively bonded composite joints with highly toughened epoxy adhesive under mixed mode conditions

Yousuke Kouno [a], Makoto Imanaka [b,*], Ryutaro Hino [c], Masaki Omiya [d], Fusahito Yoshida [e]

[a] Western Region Industrial Research Center, Hiroshima Prefectural Technology Research Institute, Agaminai Kure-shi, Hiroshima, 737-0004, Japan
[b] Osaka University of Education, 4-698-1 Asahigaoka Kashiwara, Osaka, 582-8582, Japan
[c] Department of Materials and Production Engineering, Hiroshima University, 1-4-1 Kagamiyama Higashi-Hiroshima, Hiroshima, 739-8527, Japan
[d] Department of Mechanical Engineering, Keio University, 3-14-1 Hiyoshi, Kohoku-ku, Yokohama, Kanagawa, 223-8522, Japan
[e] Institute of Engineering, Hiroshima University, 1-4-1 Kagamiyama Higashi-Hiroshima, Hiroshima, 739-8527, Japan

ARTICLE INFO

Keywords:
Adhesively bonded CFRP joint
Mixed-mode fracture
R-curve
Toughened epoxy adhesive

ABSTRACT

The fracture toughness of an adhesively bonded carbon fiber reinforced plastic joint under mixed mode (I and II) conditions was determined by means of the Fernlund–Spelt type double cantilever beam (DCB) test, where a rubber-modified epoxy adhesive was used. The *R* curves were determined by calculating the energy release rates, G_I and G_{II}, based on the beam theory, along with a finite element analysis. The total energy release rate G_T (= G_I + G_{II}) strongly depended on the I–II mixed mode. This means that it remarkably increased with increasing mode-II component; furthermore, it varied with crack growth from G_{TC} (at the onset of cracking) to G_{TS} (at the steady crack-propagation region). The difference between G_{TC} and G_{TS} increased with the increase in the mode II component. Such *R*-curve characteristics were discussed based on observation of the fracture surfaces with a scanning electron microscope and the corresponding crack propagation-path behavior.

1. Introduction

Carbon fiber reinforced plastics (CFRPs) are increasingly used in many fields of industries, such as automotive and aerospace, because of their high strength-to-weight and stiffness-to-weight ratios. For constructing CFRP structures, the adhesive-bonding technology plays a vital role, because it has advantages over the conventional mechanical joints, such as bolted and riveted joints. For the safety design of CFRP constructions, it is important to know the strength characteristics of adhesive joints.

In the adhesive layer some flaws, such as micro cracks and voids, are usually induced during bonding process, and it is very difficult to eliminate these defects. The presence of these defects reduces the strength of the joint. Hence, it is important to evaluate the strength of the joints when micro cracks exist in the adhesive layer. Usually, adhesive joints, such as lap joints, are subjected to tensile and shear stresses in the adhesive layer. Therefore, it is important to evaluate the fracture toughness of adhesive joints under the mixed tension–shear mode condition (mixed mode I and II). For the mixed mode conditions, several testing methods of the fracture toughness of adhesive joints have been proposed previously [1–4]. For bonded beams, the cracked lap shear (CLS) [5,6] and double cantilever beam (DCB) tests [7,8] are commonly used. However, the mixed mode ratios G_{II}/G_T (G_T : total energy release rate and G_{II}: mode II energy release rate) in these tests are rather limited, that is, the DCB and CLS modes are close to mode I and mode II, respectively.

For a wide range of the mixed-mode ratios, the mixed mode bending (MMB) test was performed by many researchers [3,9,10]. However, it is difficult to observe the growing crack length in MMB tests when the crack length is long, because the distance from the crack tip to the load point is limited in this type of test. When using a highly toughened adhesive, in which the stress–strain response is highly nonlinear, a crack grows stably in the adhesive layer with increasing load and final fracture occurring after a long crack propagation. For such a case, the MMB test is no longer applicable.

To conduct a mixed-mode fracture toughness test for a case of relatively long crack growth, Fernlund and Spelt [11] proposed a special loading system of a mechanical-link jig, which ensures sufficient distance from the crack tip of the specimen to the fixture point. By using this testing apparatus, the *R*-curves of several types of adhesive joints were obtained [4,11,12,14–17]. However, in most of the previous experiments, the mixed mode ratio range was not wide enough

* Corresponding author.
E-mail address: imanaka@cc.osaka-kyoiku.ac.jp (M. Imanaka).

https://doi.org/10.1016/j.ijadhadh.2020.102762

Available online 12 November 2020

Table 1
Mechanical properties of adhesive and adherend.

Adherend (Unidirectional CFRP)								
Young's modulus (GPa)			Poisson's ratio			Shear modulus (GPa)		
E_{11}	E_{22}	E_{33}	ν_{12}	ν_{23}	ν_{31}	G_{12}	G_{23}	G_{31}
130	9.9	9.9	0.31	0.21	0.02	4.0	7.5	4.0
Adhesive (Filmy type epoxy adhesive)								
Young's modulus (GPa)							Poisson's ratio	
E							V	
1.81							0.34	

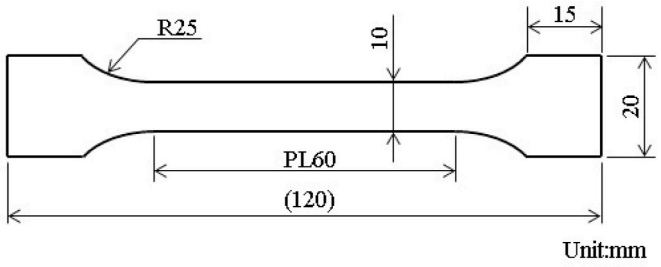

Fig. 1. Shape and sizes of dumbbell specimen for tensile test (Thickness = 3.0 mm).

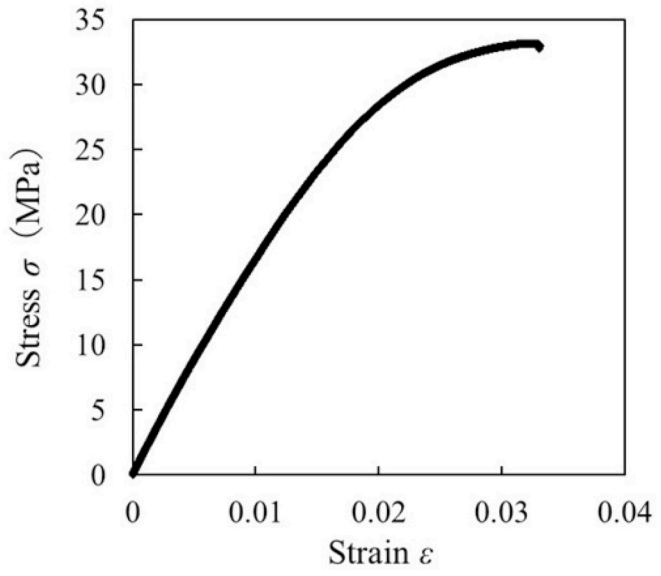

Fig. 2. Stress-strain curve of the bulk adhesive.

($0 \leq G_{II}/G_T < 0.6$), and there were very few mode-II dominant data [13,14,18].

In this study, fracture toughness tests were conducted for highly toughened (rubber-modified epoxy) adhesive CFRP joints under a wide range of mixed mode condition ($0 \leq G_{II}/G_T \leq 0.8$) using the Fernlund–Spelt type loading apparatus. In-situ observation of crack propagation, including crack-length measurement, was carried out with an area-scan camera. From the experiment, it was found that the *R*-curve behavior is strongly influenced by the mixed mode ratio. By performing the surface-roughness measurement and scanning electron microscope (SEM) observation of the fracture surface, the mode-ratio dependent damage mechanisms, which are directly related to the *R*-curve characteristics, are discussed.

2. Materials

Unidirectional CFRP prepreg sheets with a nominal thickness of 0.20 mm were used as an adherend of the DCB joint. The fiber of the CFRP was TR50S and the matrix resin was #350, Mitsubishi chemical. The unidirectional CFRP prepregs were stacked as $[0^\circ]_{40}$, then cured in autoclave under an applied pressure of 0.2 MPa and a temperature of 130°*C*. The orthotropic mechanical properties of the composite are listed in Table 1. A rubber-modified epoxy adhesive film, (AF163-2U, nominal thickness of 0.14 mm, 3 M) was used for the DCB specimen.

A tensile test was conducted to obtain the mechanical properties of the adhesive using bulk specimens. The preparation method of the specimen is as follows: The adhesive films were stacked in 24 layers on the release-treated metallic plate, which was placed in a vacuum bag for a few minutes to avoid air inclusions. Then, it was clamped between release-treated steel plates via 3 mm thickness gauges and cured at 120°*C* for 1 h. After cooling to the room temperature, the bulk adhesive plate was trimmed into a dumbbell shape specimen. The shape and dimensions of the specimen are shown in Fig. 1.

A quasi static tensile test was conducted using a tensile test machine (AG-Xplus, Shimadzu) at room temperature and the test speed of 0.5 mm/min, where the strain was measured with an extensometer (SIE-560SA, Shimadzu). The stress–strain curve of the bulk adhesive specimen is shown in Fig. 2, wherein some non-linearity is observed. Young's modulus was obtained from the slope of the elastic region of stress-strain curve, as presented in Table 1.

3. Experimental procedure

3.1. Preparation of adhesively bonded joint specimens

The adhesively bonded DCB specimen used for the mixed mode fracture test is shown in Fig. 3. The preparation of the specimen was as follows. Prior to bonding, the surface polishing with emery paper #180, then the abrasive surfaces were cleaned with acetone to remove dust, oil, and release agents. Two layers of the film adhesive were stacked together with the aid of vacuum bagging to avoid air inclusions. The initial crack of the specimen was introduced by inserting 0.01 mm thick metal film coated with a release agent. Two PTFE films were used to control the adhesive thickness, resulting a nominal value of 0.2 mm. The assembled specimen plates were clamped and cured in the thermostatic chamber at 120°*C* for 1 h. To observe the crack propagation behavior clearly, the side edge of the joints was polished with emery paper #1500 along the adhesive layer after removing the excess adhesive.

3.2. Fracture toughness test

Fracture toughness tests were conducted using the Fernlund–Spelt loading jig [11] as shown in Fig. 4, wherein, the cross-sectional dimensions of the links and the connecting rods were large enough to consider these parts as rigid bodies. Hence, this jig enables to conduct the DCB fracture toughness tests under a wide range of mixed mode conditions.

The DCB was supported at upper- and lower-layer points, and it was subjected to loads F_1 and F_2 by two pins installed at the upper- and lower surfaces of the beam end, as schematically illustrated in Fig. 4. Hence, the applied loads F_1 and F_2 for a given jig load F were determined by the pin arrangement, S_1-S_4, in the jig beams, as follows:

$$F_1 = F\frac{S_2}{S_3}, \tag{1}$$

$$F_2 = F\frac{S_1 S_4}{S_3(S_3 + S_4)}, \tag{2}$$

where S_1, S_2, S_3 and S_4 are the lengths of the links as shown in Fig. 4.

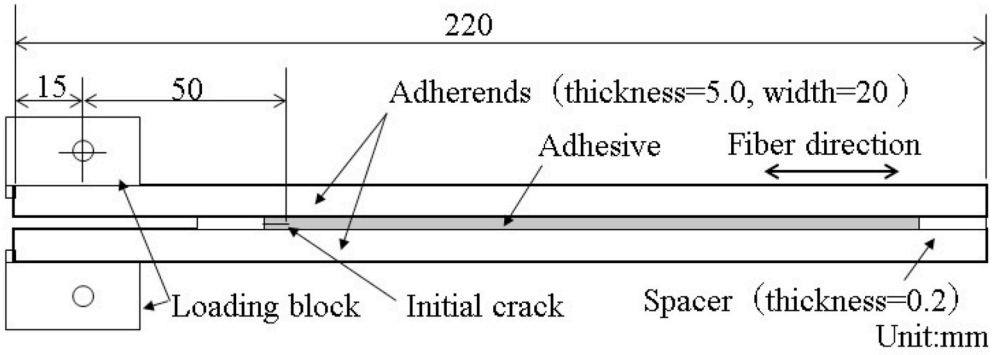

Fig. 3. Shape and sizes of adhesively bonded DCB specimen.

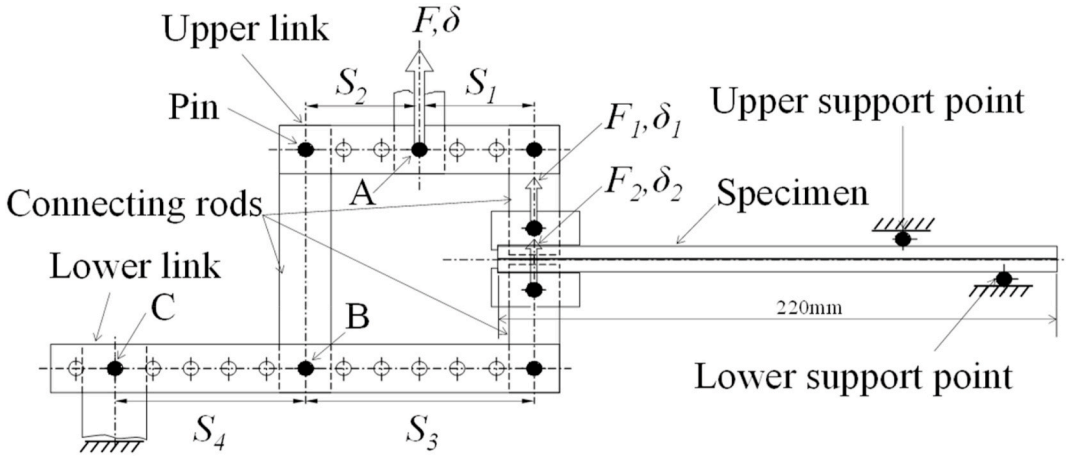

Cross section of upper and lower links	width:20mm, thickness:20mm
Cross section of connecting rods	width:20mm, thickness:6mm

Fig. 4. Schematic of multiple linked load jig proposed by Fernlund and Spelt [11].

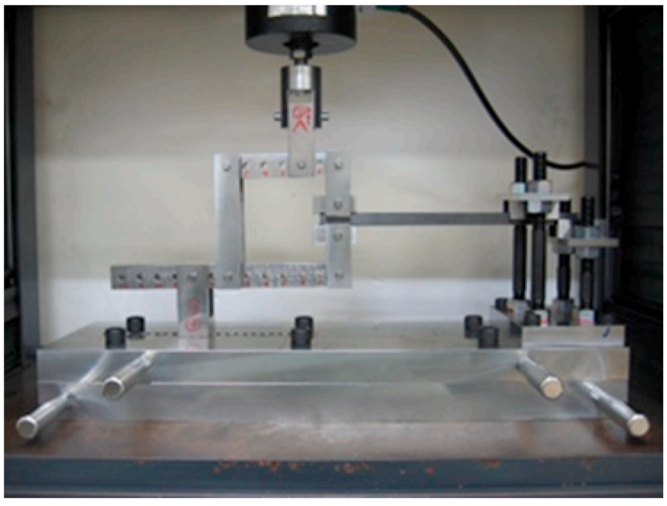

Fig. 5. Experimental setup for mode ratio (G_{II}/G_T=0.55).

Note in this type of DCB test, several mixed mode ratios (G_{II}/G_T) were fixed by just changing the pin arrangement in the jig, because, as will be discussed later (see Section 4), the mixed mode ratio is given as a function of F_1 and F_2. Fig. 5 shows the experimental setup for a mixed mode ratio ($G_{II}/G_T = 0.55$).

Fracture tests were conducted with a test machine (AG-100NE, Shimadzu) at a cross head speed of 0.5 mm/min. Though the crosshead speed was the same as that of the dumbbell specimen, there were a couple of orders of magnitude difference between the strain rate of the dumbbell specimen and the strain rate of the adhesive layers in the fracture test.

The load F and the crosshead movement δ were measured by a load-cell and an encoder mounted on the test machine, respectively, and they were recorded during the test with a frequency of 5 Hz. The crack tip image was recorded using an optical microscope camera mounted on an XYZ stage, wherein the XYZ table was moved so that the crack tip was positioned at the center of the microscope. The crack growth length was measured by the displacement of the stage using a linear gauge (LG-1100 N, Mitsutoyo).

3.3. Microscopy observations and surface-roughness determination

The fracture surfaces were observed with a SEM (JSM-6510A, JEOL). Prior to examination, the fracture surfaces were coated with an Au layer.

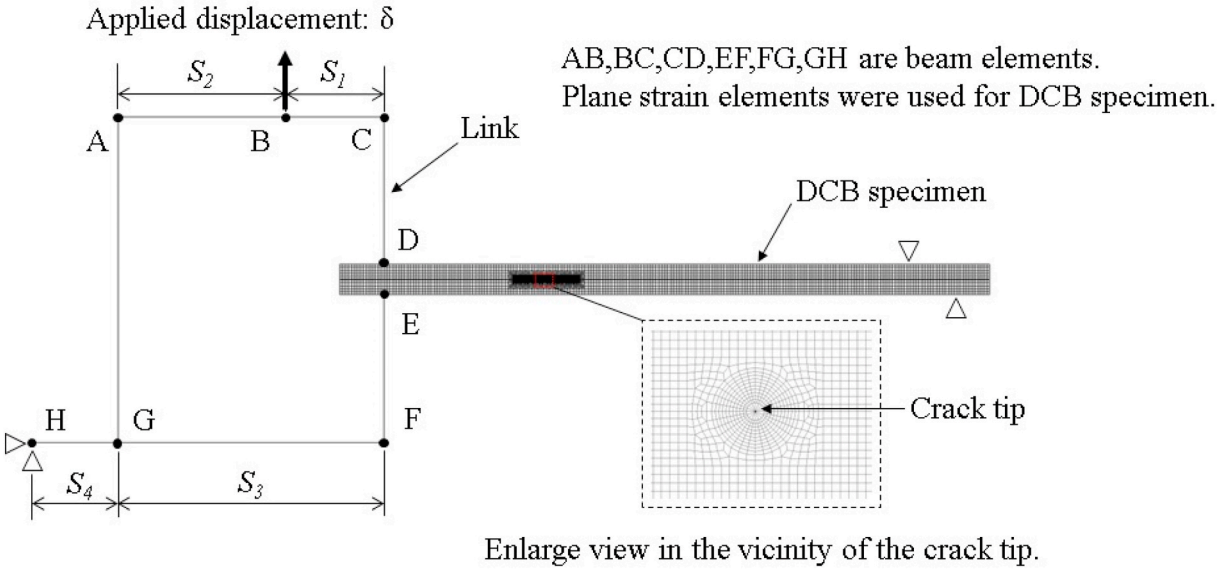

Fig. 6. Boundary conditions and mesh pattern for FE analysis.

The macroscopic surface morphology was observed using the digital microscope (VR-3050, Keyence). By using this microscope, the surface roughness was determined by means of the area roughness parameter *Sa* (arithmetical mean height) which is the extension of *Ra* (arithmetical mean height of a line) to a surface. It expresses the difference in height of each point compared to the arithmetical mean height of surface.

4. Evaluation method of fracture toughness and mode partitioning

4.1. Simple beam theory

Based on the Bernoulli–Euler beam theory, neglecting the adhesive layer, Fernlund and Spelt [11] proposed the following equation of the total energy release rate in the DCB test for given loads F_1 and F_2:

$$G=\frac{P^2}{2B}\frac{dC}{da}=\frac{6(F_1a)^2}{B^2Eh^3}\left[1+\left(\frac{F_2}{F_1}\right)^2-\frac{1}{8}\left(1+\left(\frac{F_2}{F_1}\right)\right)^2\right], \tag{3}$$

where B and h are the width and thickness of the adherend, respectively, a is the crack length, and E is the Young's modulus of the adherend. As the adherend was used unidirectional CFRP, the Young's modulus E was replaced with E_{11}.

The phase angle of loading was defined as:

$$\psi=\arctan\left[\frac{\sqrt{3}}{2}\frac{\left(\frac{F_1}{F_2}+1\right)}{\left(\frac{F_1}{F_2}-1\right)}\right] \tag{4}$$

The energy release rates in mode I and II are given by:

$$G_I=G\left[\frac{1}{1+\tan^2(\psi)}\right] \tag{5}$$

$$G_{II}=G\left[\frac{\tan^2(\psi)}{1+\tan^2(\psi)}\right] \tag{6}$$

4.2. Beam theory considering adhesive layer

Fernlund and Spelt [12] further considered the elastic deformation of the adhesive layer based on the theory of a beam placed on an elastic foundation, as follows. The external forces F_1 and F_2 are separated into mode I component f_1 and mode II component f_2, respectively, as

$$f_1=\frac{F_1-F_2}{2}, \tag{7}$$

$$f_2=-\frac{F_1+F_2}{2}. \tag{8}$$

Then the energy release rate, considering adhesive thickness t, is given by the equation:

$$G=\frac{P^2}{2B}\frac{dC}{da}=\frac{12a^2}{B^2E(h-t)^3}\left[f_1^2\Phi_I^2+\frac{3}{4}f_2^2\Phi_{II}^2\right], \tag{9}$$

where a is crack length, and E and h are elastic modulus of the adherend and thickness, respectively. Φ_I and Φ_{II} are given by the equations:

$$\Phi_I=1+0.667\frac{h}{a}\left[\left(1-\frac{t}{h}\right)^3\left[1+\frac{t}{h}\left(\frac{2E}{E_a}-1\right)\right]\right]^{0.25}, \tag{10}$$

$$\Phi_{II}=1+0.206\frac{h}{a}\sqrt{\left[1-\frac{t}{h}\right]\left[1+\frac{2tE\alpha}{G_ah}\right]}, \tag{11}$$

where $\alpha=2.946$ is a calibration constant determined by a finite element (FE) analysis [8]. E_a and G_a are the elastic and shear modulus of adhesive, respectively. The phase angle is given by the following equation:

$$\psi=\arctan\left[\frac{\sqrt{3}}{2}\frac{f_2\Phi_{II}}{f_1\Phi_I}\right]. \tag{12}$$

In addition, the total energy release rate G is separated into the individual energy release rates G_I and G_{II} are calculated by Eqs (5) and (6) using the phase angle ψ.

4.3. FE analysis

A two dimensional (2D) linear elastic FE analysis was conducted with the FE code MSC-marc. In this analysis, the loading devices were modeled by a combination of beam and links. The DCB specimen was modeled with plane strain four node quadrilateral elements. The adhesive layer was meshed with twelve elements across the thickness. The crack was introduced by double nodes along edges of elements on the middle of adhesive thickness. The size of the element at the crack tip was 0.015 mm. The overall mesh and boundary conditions are illustrated in Fig. 6. Load F was applied at point B. The movement of the specimen was constrained in the vertical direction at its right end.

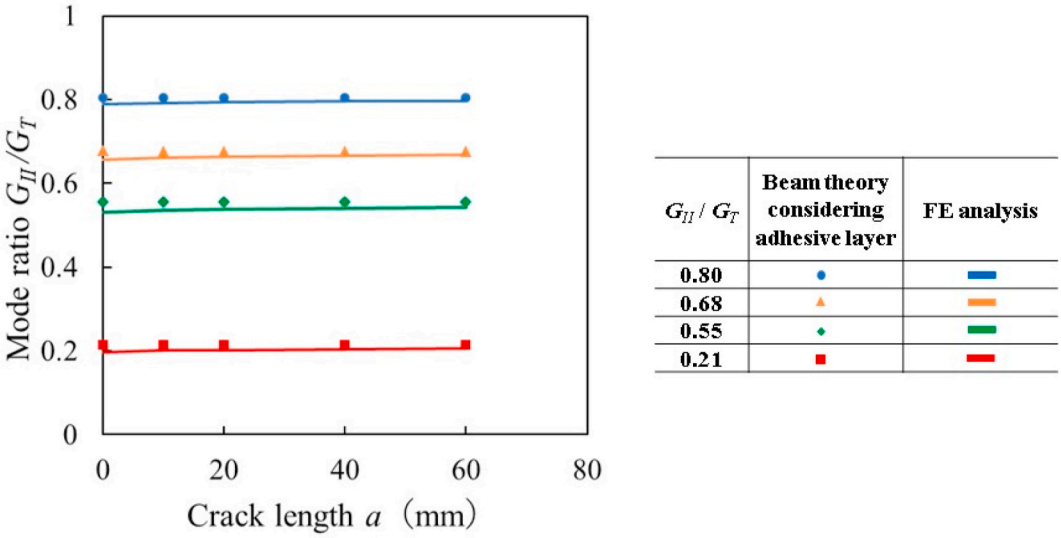

Fig. 7. Relationship between mode ratio and crack extension.

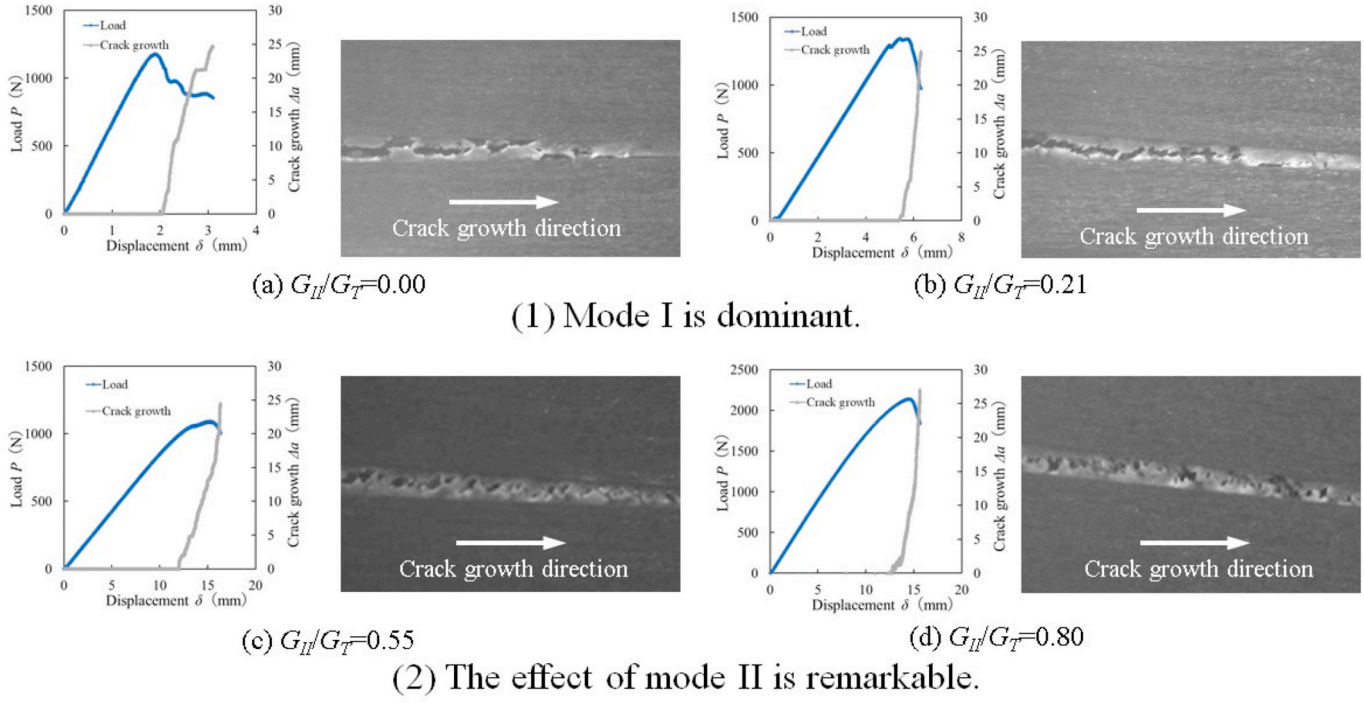

Fig. 8. Load-displacement and crack extension-displacement curves and microscopic images of adhesive layer for typical mode ratios.

As shown in Fig. 6, though F_1 and F_2 could be calculated by equations (1) and (2), the FE analysis using link elements was conducted. This was because the fracture toughness value could be immediately obtained from the applied load. To confirm the validity of FE analysis using link elements, it was confirmed that the values F_1 and F_2 calculated from the FE analysis agreed with the values obtained from the given F according to the equations (1) and (2).

The mechanical properties used in this simulation are presented in Table 1. Besides, geometric nonlinearity is considered in this analysis.

To validate the analytical expressions for G_I and G_{II} derived in the previous section, theoretical value was compared with that derived from the FE analysis. In the FE analysis, the energy release rate components were calculated using the virtual crack closure technique (VCCT), for cases of low applied load wherein the influence of geometrical nonlinearity on the calculation was small. The analysis was conducted under the typical crack length to confirm for influence of crack length on energy release rate. The mode ratio G_{II}/G_T, as defined by the beam theory and FE analysis is presented in Fig. 7.

As shown in this figure, it was confirmed that the mode ratio G_{II}/G_T, shows a mainly constant value throughout the crack length. This figure also shows that the mode ratio obtained by the FE analysis agrees well with that calculated by the beam theory irrespective of crack length.

When the applied load is large, the value calculated from VCCT may have an error in estimating the energy release rate due to the influence of geometrical nonlinearity. Therefore, the J-integral value was used as the energy release rate value G in spite of the elastic analysis, wherein the J-integral was performed along an arbitrary path encircling the crack tip of the adhesive layer.

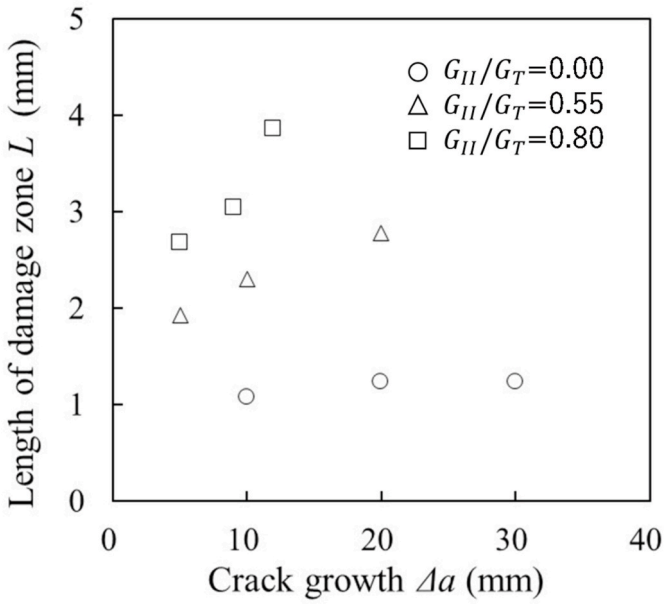

Fig. 9. Relationship between length of damage zone and crack growth.

5. Experimental results and discussion

5.1. Fracture toughness

Typical load vs. displacement curves and crack growth behaviors for various mode ratios are shown in Fig. 8. Additionally, microscopic images of side views of the adhesive layer in the vicinity of the crack tips for crack lengths of 0.2–5.0 mm are also indicated. The direction of crack propagation was from left to right. As shown later, microcracks occur in front of the crack in accordance to the increase in Mode II component. Here, microcracks generated discontinuously at the crack tip were not regarded as cracks, but the crack length was determined with the tip of the microcracks connected to the main crack at the crack tip. From the microscope images, approximate crack growth rates were measured and ranged from approximately 0.07 mm/s to 0.18 mm/s.

As shown in this figure, the load-displacement curves are almost linear up to the maximum load.

In the cases of $G_{II}/G_T = 0$ and 0.21, the crack propagation initiates at the maximum load, and then the crack grows with decreasing load. In the cases of $G_{II}/G_T = 0.55$ and 0.80, the crack propagation starts before the load reaches the maximum load. As shown in Fig. 8a and b, in the cases of $G_{II}/G_T = 0.00$ and 0.21, the crack propagates almost straightly along the adhesive-layer line, whereas in the cases of $G_{II}/G_T \geq 0.55$ the crack progresses while the microcracks are connected to the front of the main crack, as shown in Fig. 8c and d. In the case of $G_{II}/G_T = 0.55$, microcracks were observed across the entire adhesive thickness. The microcracks were inclined at approximately 45° with respect to the adhesive layer. In the case of $G_{II}/G_T = 0.80$, coalescence of microcracks was observed at the front of the crack tip as shown in Fig. 8d. Blackman et al. [19] observed a similar behavior in the vicinity of the crack tip under mode II loading condition. A new finding in this work is that the crack propagation behavior under shear-dominant mixed mode conditions ($G_{II}/G_T \geq 0.55$) is almost the same as that under the pure shear mode. Besides, every fracture mode was cohesive fracture.

Based on the recording images of damage zone due to crack growth as in Fig. 8, the relationship between the length of damage zone and the crack growth was shown in Fig. 9. In this figure, the damaged zone means the area where stress whitening and microcracks are confirmed in front of the crack tip, and the length of the damage is the distance from the crack tip to the end of the damage zone.

This figure shows that the change in the damage length is small with the increase in the crack length under mode I loading, and also shows that both of the damage length and the rate of increase in damage length due to the crack growth increase with the increase in mode II component.

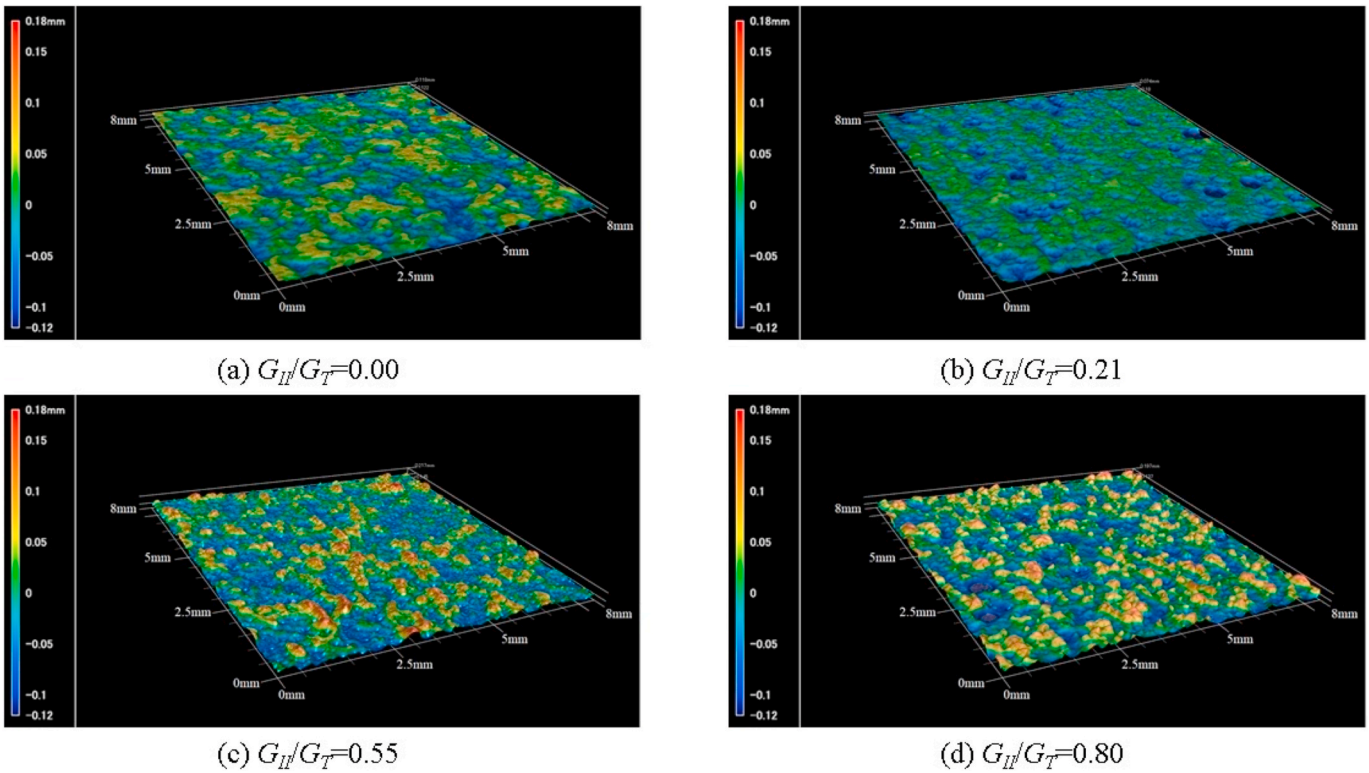

Fig. 10. Microscopic view of fracture surfaces for typical mode ratios.

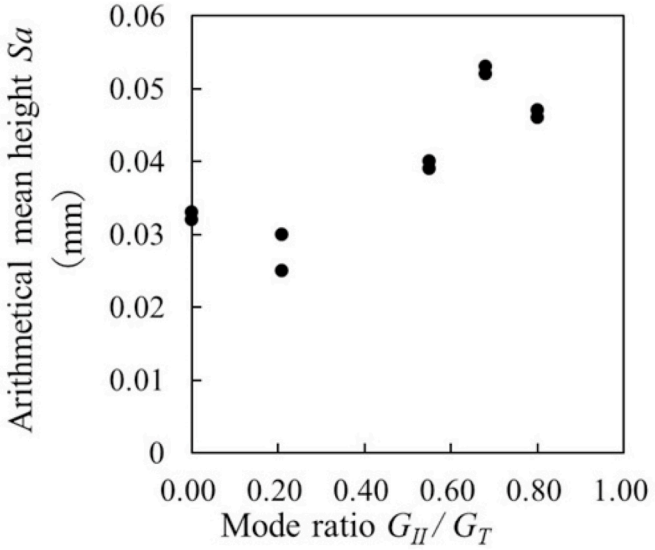

Fig. 11. Relationship between surface roughness and mode ratio.

Typical 3D digital microscopic images of the fracture surfaces for various mode ratios are shown in Fig. 10. In this figure, the crack growth direction is left to right and the observation area is 8 × 8 mm ahead of the initial crack tip. The contour level indicates the height of the fracture surface.

As shown in Fig. 10a and b, the fracture surfaces in the cases of $G_{II}/G_T = 0$ and 0.21 are relatively flat. This implies that the crack propagates almost straight along the adhesive-layer line, as shown in Fig. 8a and b. In the cases of $G_{II}/G_T = 0.55$ and 0.80, the crests of the fracture surfaces are significantly higher than those in the cases of $G_{II}/G_T = 0$ and 0.21, as shown in Fig. 10. This also implies that the crack progresses while the microcracks are connected to the front of the main crack, as shown in Fig. 8c and d. When $G_T = 0.80$, the surface roughness is the highest among all the tests. This result indicates that the microcracks coalesce with each other during crack propagation in the mode II predominant condition.

The surface roughness parameters S_a calculated from the above height data of fracture surface for various mode ratios are summarized in Fig. 11. This figure shows that S_a increases with the increase in the mode II component. This is because the crack propagation path develops a more complicated shape as the mode II component increases.

5.2. R-curve behavior

Fig. 12 shows the relation between the total energy release rate, G_T, and crack growth, Δa, for various mode ratios, wherein G_T was calculated by the aforementioned three methods (simple beam theory, beam theory considering adhesive layer, and FE analysis). The energy release rates calculated by the beam theory considering the adhesive layer are almost the same as those in the FE calculation results, whereas the results calculated by the simple beam theory are apparently lower than those obtained with the FE calculations. The difference in G_T calculation between the simple beam theory and the FE method is more significant at a higher mixed-mode ratio G_{II}/G_T. Hafiz et al. [13] also reported for an adhesively bonded steel joint with a brittle adhesive that the energy release rate calculated by FEM agrees well with the energy release rate calculated by equation (9) considering the adhesive layer. From these results, it would be concluded that the consideration of the adhesive layer is of vital importance for accurate G_T calculation.

Fig. 12 indicates that G_T was almost constant independently of the crack length in the cases of $G_{II}/G_T = 0$ and 0.21, whereas in the cases of $G_{II}/G_T = 0.55$, 0.68, and 0.80, it increases with the crack growth up to an approximately 10 mm crack length, and then it saturates. Azari et al. [14] also reported that the slope of the *R*-curve increased with the increase in the proportion of mode II. Such a trend of *R*-curves agrees with that of the relationship between length of damage zone and crack growth as in Fig. 9.

To observe the mixed-mode dependent *R*-curve characteristics more clearly, Fig. 13 illustrates the relationship between the total energy release rate G_T and the mode ratio G_{II}/G_T, along with the corresponding FE analysis results. In this figure, G_{TS} denotes the steady state energy release rate over the plateau region of the *R*-curve (see Fig. 12), and G_{TC} is the critical energy release rate at the crack initiation. The energy release rates, G_{TC} and G_{TS}, increase with the increase in the mode II component, and the difference between G_{TC} and G_{TS} becomes larger with increasing G_{II}/G_T. Such a tendency is also confirmed in data of other papers as shown in this figure.

Generally, in adhesive joints under mode-I loading, the stress multiaxiality is high at the crack tip. Thus, the plastic region is small and, as the mode II component increases, the stress multiaxiality decreases and the plastic region expands. Therefore, fracture toughness increases with the increase in the mode II component [13,15,18,19]. Furthermore, it has been also observed that an increase in mode II component creates

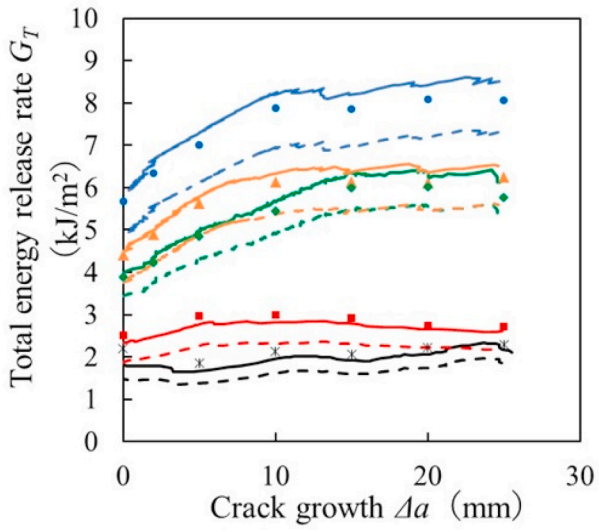

Experimental value of the total energy release rate were calculated by,
(a) Simple beam theory
(b) Beam theory considering adhesive layer
(c) FE analysis

G_{II}/G_T	(a)	(b)	(c)
0.80	- -	———	●
0.68	- -	———	▲
0.55	- -	———	◆
0.21	- -	———	■
0.00	- -	———	*

Fig. 12. Relationship between total energy release rate and crack growth with various mode ratios.

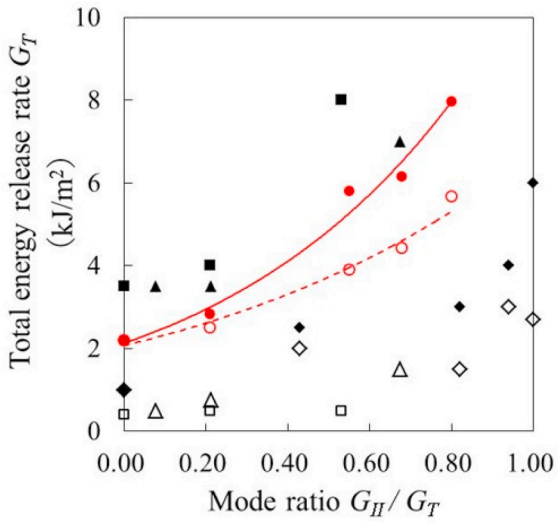

Experimental value of the total energy release rate were calculated by FE analysis.
(a) Steady state energy release rate :G_{TS}
(b) Crack initiation energy release rate :G_{TC}

	(a)	(b)
Experimental plot	●	○
Curve fit	——	----

Data from the reference paper lists.

Reference number	(a)	(b)	Adhesive and adherend
14	▲	△	Paste type epoxy adhesive/Aluminum alloy
15	■	□	Paste type epoxy adhesive/Aluminum alloy
18	◆	◇	Film adhesive(FM300-2M:Cytec Engineered Materials)/CFRP

Fig. 13. Relationship between total energy release rate and mode ratio.

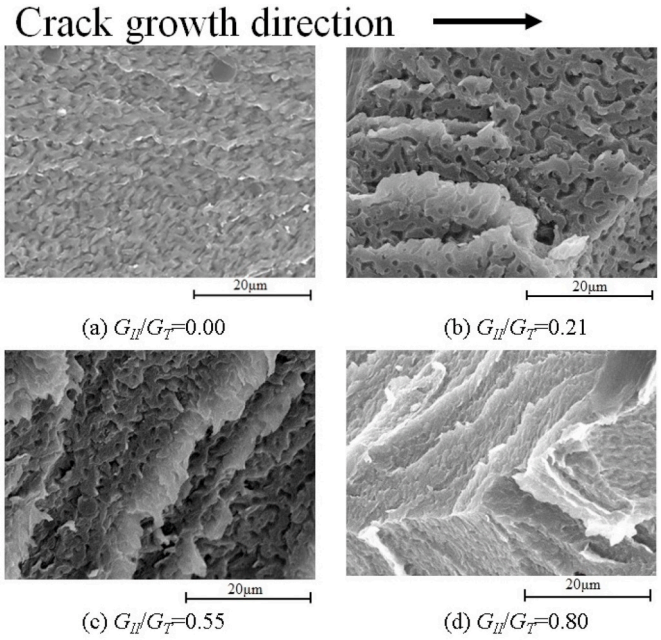

Fig. 14. SEM observation of fracture surfaces for typical mode ratios.

microcracks inclined toward the interface in the vicinity at the crack tip [18,19]. Thus, the increase in the mode II component forms a complicated damage area at the crack tip where a plastic area and a microcrack overlap.

Some researchers [12,15] have explained the reason why the difference between G_{TC} and G_{TS} increases with the increasing mode II component from the viewpoint of the increase in the complicated damage zone due to the increase in the mode II component. However, the expansion of the plastic and damage zones contributes to the increase in both G_{TC} and G_{TS}. Therefore, only these reasons are insufficient to explain why the increase in the mode II component increases the slope of *R*-curve, in other words, the difference between G_{TC} and G_{TS}. Besides the plastic and damage-zone effects, we can assume that the difference between both G_{TC} and G_{TS} relates to the complicated crack propagation path appearing in a mode-II-dominant fracture (see Fig. 11, wherein surface roughness increased in mode II component). Such a complicated crack path would increase the crack growth resistance. This would be a possible explanation for the *R*-curve characteristic wherein the difference between G_{TC} and G_{TS} increases with the increase in mode II component.

5.3. SEM observation of fracture surfaces

Fig. 14a – d show the SEM observation images of the fracture surfaces for the mode ratios of $G_{II}/G_T = 0$, 0.21, 0.55, and 0.80, respectively, which correspond to those in Fig. 10. As shown in Fig. 14a, many voids of approximately 1 μm in diameter were observed on the relatively flat surface. These voids would be induced by cavitation of the rubber particles contained in the adhesive due to the high tri-axial tensile stress under mode-I loading condition [20–22]. In Fig. 14b, similar voids were also observed under $G_{II}/G_T = 0.21$ because this was still a I-dominant condition. However, in this case, different from the pure mode I ($G_{II}/G_T = 0$), a pleated deformation was observed on the surface. This was a result of the mode II (shear) component. The pleated surface deformation became more significant with an increasing mode II component (compare Fig. 14b: $G_{II}/G_T = 0.21$ and c: $G_{II}/G_T = 0.5$). Note that even under a high mode-II condition, many voids were still observed. On the fracture surface for a case of the highest mode II component, $G_{II}/G_T = 0.80$, as shown in Fig. 14d, a sharply ridged deformation was observed, wherein the growth of voids was suppressed under the low triaxial tensile-stress condition.

6. Conclusions

Fracture toughness tests for adhesively bonded CFRP joints under mixed I and II mode conditions were conducted by means of the Fernlund–Spelt DCB test, where a highly toughened epoxy adhesive was used. The main findings of this study are as follows:

1. The total energy release rate G_T increased with the increase in the mode II component. In the mode ratios $G_{II}/G_T = 0$ and 0.21, G_T was almost constant irrespective of crack length, whereas in the cases of $G_{II}/G_T = 0.55$, 0.68 and 0.80, G_T increased up to approximately 10 mm crack length, then it saturated for further crack growth.
2. The difference between G_{TC} (= G_T at the onset of crack growth) and G_{TS} (= G_T at the steady state) increases with the increase in mode II component. This reason may occur because the crack propagation path has a more complicated shape with the increase in mode II component, and the complicated crack propagation path increases the crack growth resistance. Reflecting such crack growth behavior,

the surface roughness S_a increased with the increase in mode II component. This is because the crack propagation path develops a more complicated shape as the mode II component increases.

3. From SEM observation of the fracture surfaces, under the pure mode I condition ($G_{II}/G_T = 0$), many voids induced by a high triaxial tensile stress were observed on the relatively flat fracture surface. As the mode II component increased, the pleated deformation became more dominant, wherein many voids were still observed until the mode ratio G_{II}/G_T reached 0.55. On the fracture surface for $G_{II}/G_T = 0.80$ (where the mode II component was the highest), a sharply ridged deformation was observed, wherein the growth of voids were suppressed under the low triaxial tensile-stress condition.

Acknowledgment

We would like to thank Editage (www.editage.com) for English language editing.

References

[1] Dillard DA, Dillard DA, Blackman B, Adams RD. Other mixed mode adhesive fracture tests specimens. In: da Silva LFM, editor. Testing adhesive joints—best practices. Wiley-VCH; 2012. p. 194–201.
[2] Pong JHL, Dillard DA, Blackman B, Adams RD. Compact mixed mode (CMM) fracture test method. In: da Silva LFM, editor. Testing adhesive joints—best practices. Wiley-VCH; 2012. p. 201–12.
[3] Davies P. Mixed mode bending (MMB) with a Reeder and Crew fixture. In: da Silva LFM, Dillard DA, Blackman B, Adams RD, editors. Testing adhesive joints—best practices. Wiley-VCH; 2012. p. 212–6.
[4] Ameli A, Azari S, Papini M, Spelt JK. Mixed mode fracture testing. In: da Silva LFM, Dillard DA, Blackman B, Adams RD, editors. Testing adhesive joints—best practices. Wiley-VCH; 2012. p. 216–24.
[5] Dattaguru B, Everett Jr RA, Whitcomb JD, Johnson WS. Geometrically nonlinear analysis of adhesively bonded joints. J Eng Mater Technol 1984;106:59–65. https://doi.org/10.1115/1.3225677.
[6] Mangalgiri PD, Johnson WS. Preliminary design of cracked-lap shear specimen thickness for determination of interlaminar toughness. J Compos Technol Res 1986;8:58–60. https://doi.org/10.1520/CTR10323J.
[7] Azari S, Papini M, Schroeder JA, Spelt JK. The effect of mode ratio and bond interface on the fatigue behavior of a highly-toughened epoxy. Eng Fract Mech 2010;77:395–414. https://doi.org/10.1016/j.engfracmech.2009.09.011.
[8] Azari S, Papini M, Schroeder JA, Spelt JK. The effect of adhesive thickness on fatigue and fracture of toughened epoxy joints-Part 1. Experiments Eng Fract Mech 2011;78:153–62. https://doi.org/10.1016/j.engfracmech.2010.06.025.
[9] Shahverdi M, Vassilopoulos AP, Keller T. Mixed-mode quasi-static failure criteria for adhesively-bonded pultruded GFRP joints Composites. Part Accel 2014;59:45–56. https://doi.org/10.1016/j.compositesa.2013.12.007.
[10] Stamoulis G, Carrere N, Congnard JY, Davis P, Badulescu C. On the experimental mixed mode failure of adhesively bonded metallic joints. Int J Adhesion Adhes 2014;51:148–58. https://doi.org/10.1016/j.ijadhadh.2014.03.002.
[11] Fernlund G, Spelt JK. Mixed-mode fracture characterization of adhesive joints. Compos Sci Technol 1994;50(4):441–9. https://doi.org/10.1016/0266-3538(94)90052-3.
[12] Fernlund G, Spelt JK. Mixed mode energy release rates for adhesively bonded beam specimens. J Compos Technol Res 1994;16(3):234–43. https://doi.org/10.1520/CTR10412J.
[13] Hafiz TA, Abdel Wahab MM, Crocombe AD, Smith PA. Mixed-mode fracture of adhesively bonded metallic joints under quasi-static loading. Eng Fract Mech 2010;77:3434–45. https://doi.org/10.1016/j.engfracmech.2010.09.015.
[14] Azari S, Eskandarian M, Papini M, Schroeder JA, Spelt JK. Fracture load predictions and measurements for highly toughened epoxy adhesive joints. Eng Fract Mech 2009;76:2039–55. https://doi.org/10.1016/j.engfracmech.2009.05.011.
[15] Ameli A, Papini M, Schroeder JA, Spelt JK. Fracture R-curve characterization of toughened epoxy adhesive. Eng Fract Mech 2010;77:521–34. https://doi.org/10.1016/j.engfracmech.2009.10.009.
[16] Chaves FJP, de Moura MFSF, da Silva LFM, Dillard DA. Numerical validation of a crack equivalent method for mixed-mode I + II fracture characterization of bonded joints. Eng Fract Mech 2013;107:38–47. https://doi.org/10.1016/j.engfracmech.2013.05.008.
[17] Xie DE, Chung J, Waas AM, Shahwan KW, Schroeder JA, Boeman RG, kunc V, Klett LB. Failure analysis of adhesively bonded structures: from coupon level data to structural level predictions and verification. Int J Fract 2005;134:231–50. https://doi.org/10.1007/s10704-005-0646-y.
[18] Mohan J, Ivanković A, Murphy N. Mixed-mode fracture toughness of co-cured and secondary bonded composite joints. Eng Fract Mech 2015;134:148–67. https://doi.org/10.1016/j.engfracmech.2014.12.005.
[19] Blackman BRK, Kinloch AJ, Paraschi M. The determination of the mode II adhesive fracture resistance, GIIC, of structural adhesive joints: an effective crack length approach. Eng Fract Mech 2005;72:877–97. https://doi.org/10.1016/j.engfracmech.2004.08.007.
[20] Kinloch AJ, Shaw SJ, Tod DA, Hunston DL. Deformation and fracture behavior of a rubber-toughened epoxy:1. Microstrucuture and fracture studied. Polymer 1983;24:1341–54. https://doi.org/10.1016/0032-3861(83)90070-8.
[21] Pearson RA, Yee AF. Toughening mechanisms in elastomer-modified epoxies Part 2 Microscopy studies. J. Mat. Sci. 1986;21:2475–88. https://doi.org/10.1007/BF01114294.
[22] Bagheri R, Pearson RA. Role of particle cavitation in rubber-toughened epoxies: 1. Microvoided toughening. Polymer 1996;37:4529–38. https://doi.org/10.1016/0032-3861(96)00295-9.